

A unified framework for geometry-independent operator learning in cardiac electrophysiology simulations

Bei Zhou¹, Cesare Corrado¹, Shuang Qian¹, Maximilian Balmus^{1,2},
Angela W. C. Lee¹, Cristobal Rodero¹, Caroline Roney³,
Marco J.W. Götte⁴, Luuk H.G.A. Hopman⁴, Mengyun Qiao⁵,
Steven Niederer^{1, 2}

¹Imperial College London, London, United Kingdom.

²Alan Turing Institute, London, United Kingdom.

³Queen Mary University of London, London, United Kingdom.

⁴Amsterdam University Medical Center, Amsterdam, The Netherlands.

⁵University College London, London, United Kingdom.

Abstract

Learning biophysically accurate solution operators for cardiac electrophysiology is fundamentally challenged by geometric variability across patient-specific heart anatomies. Most existing neural operator approaches are limited to structured or weakly deformed domains, restricting their applicability to realistic atrial and ventricular geometries. Here, we introduce a unified operator-learning framework that projects inputs and outputs onto a standardised anatomical coordinate system, decoupling electrophysiological dynamics from mesh topology. This formulation enables geometry-independent learning while preserving physiologically meaningful spatial organisation, and allows predictions to be interpolated back onto patient-specific geometries for anatomical interpretation.

To support large-scale training within the framework, we develop a GPU-accelerated electrophysiology solver and generate over 300,000 high-fidelity simulations across diverse patient-specific left atrial geometries with varied pacing and conduction properties. Within this anatomical coordinate domain, we design a neural operator to predict full-field local activation time maps, achieving a mean absolute error of 5.1 ms and an inference time of 0.12 ms per sample, outperforming existing operator learning and convolutional baselines. We further validate the framework on ventricular geometries, demonstrating robust generalisation beyond the atrial setting. Together, this framework establishes a scalable foundation for fast, geometry-invariant cardiac electrophysiology modelling, with potential relevance for real-time and population-scale clinical workflows.

Introduction

Computational models of cardiac electrophysiology provide a principled framework for studying electrical wave propagation, investigating arrhythmia mechanisms, and informing patient-specific therapeutic interventions [1–3]. A central application of these models is the analysis of local activation time (LAT) maps, which characterise the spatiotemporal evolution of electrical activation across the myocardium [4–6]. Generating and analysing such LAT maps typically requires large ensembles of high-fidelity finite element method (FEM) simulations on anatomically detailed, patient-specific geometries, involving the numerical solution of coupled partial differential equations governing cardiac electrophysiology [7, 8].

Atrial fibrillation (AF) is a primary clinical setting in which such patient-specific LAT analyses are routinely required [9]. As the most common sustained cardiac arrhythmia, AF affects approximately 46.3 million individuals worldwide [10] and is a leading cause of stroke [11], heart failure [12], and sudden cardiac death [13]. Computational modelling has therefore become an important tool in AF research and clinical studies, supporting mechanistic investigation of arrhythmia drivers, evaluation of ablation strategies, and development of personalised treatment planning [14–17]. However, the substantial computational cost of FEM-based workflows, often requiring hours to days per simulation, limits their applicability in settings that demand rapid or real-time decision-making [15, 18].

Recent advances in machine learning have opened new avenues for accelerating cardiac electrophysiology simulations. Neural operators, in particular, aim to learn mappings between infinite-dimensional function spaces [19], enabling solution fields to be predicted for unseen inputs, discretisations, or geometries without retraining. Architectures such as DeepONet [20] and the Fourier Neural Operator (FNO) [21] have demonstrated strong performance on parametric partial differential equation problems. Despite this promise, most existing neural operator frameworks are developed for structured or weakly deformed computational domains, which limits their applicability to the highly irregular, patient-specific geometries encountered in cardiac modelling [22, 23]. In addition, training robust and generalisable operators requires large, high-quality simulation datasets, which remain expensive to generate using conventional electrophysiology solvers [24, 25].

Several strategies have been proposed to address anatomical variability in operator learning. Diffeomorphic mapping approaches [26], including Diffeomorphic Mapping Operator Learning (DIMON) [27], map individual geometries to a shared reference domain, enabling learning in a common representation while encoding geometry as auxiliary information. While effective for relatively simple geometries, such as the semi-spherical left ventricle, these approaches become challenging for anatomies with complex topology, such as the multi-holed left atrium, where constructing globally consistent mappings is non-trivial. Related methods, such as Geo-FNO [22], deform irregular geometries to structured domains to enable spectral learning, but the accuracy and stability of such mappings may deteriorate for highly intricate anatomical structures.

Here, we propose a framework that reformulates neural operator learning in a coordinate domain intrinsic to cardiac anatomy rather than in the space of mesh discretisations. By expressing model inputs and outputs in a shared anatomical parameterisation, electrophysiological patterns can be represented consistently across patients despite substantial geometric and topological variability. Predictions obtained in this coordinate space can subsequently be mapped back onto the original patient-specific geometry, enabling anatomically faithful reconstruction and direct clinical interpretation. In this work, we adopt the Universal Atrial Coordinates (UAC)

[28] and Universal Ventricular Coordinates (UVC) [29] systems to define such intrinsic representations for atrial and ventricular geometries, respectively. These coordinate systems preserve physiologically meaningful spatial organisation while providing a unified domain across diverse anatomies, enabling neural operators to learn spatially coherent solution mappings without sensitivity to irregular mesh connectivity or topological inconsistencies.

To support operator training within this framework, we further develop a GPU-accelerated electrophysiology simulation pipeline that enables efficient generation of high-fidelity LAT maps at scale across diverse patient-specific geometries. By integrating high-performance simulation with neural operator learning in anatomical coordinate space, our approach addresses both the computational cost of cardiac electrophysiology modelling and the geometric variability inherent in patient-specific anatomies, providing a scalable pathway toward rapid, physiology-informed inference in atrial fibrillation.

Results

Large-scale EP simulations on GPUs

We generated a comprehensive set of biophysically detailed EP simulations using a custom GPU-accelerated FEM solver applied to two independent cohorts of AF patients (Cohort A: $n = 100$; Cohort B: $n = 47$). This process constructed two large-scale datasets, Dataset A and Dataset B, respectively (see Methods). To ensure robustness across diverse anatomical and physiological conditions, for each of the 147 patient-specific LA, we simulated LAT maps from seven distinct pacing sites across the LA. At each site, we sampled 300 combinations of the key conduction parameters, the longitudinal conductivity (σ_l) and the anisotropy ratio (σ_l/σ_t), using Latin hypercube sampling [30] to cover a wide range of clinically relevant tissue properties. This yields a total of 308,700 simulated LAT maps, establishing one of the largest computational datasets of its kind for training neural operators.

All simulated LAT maps were subsequently projected onto the standardised UAC domain to obtain a consistent, geometry-independent representation. Fig. 1a illustrates an LAT map on the 3D atrial surface together with its corresponding 2D UAC projection, with the coronary sinus pacing site producing full atrial activation within 204 ms.

To assess potential cohort-level differences, we performed dimensionality reduction on the full set of UAC-projected LAT maps. High-dimensional LAT fields were first denoised using principal component analysis (PCA), and the resulting principal components were subsequently embedded using Uniform Manifold Approximation and Projection (UMAP) [31]. The 2D embedding (Fig. 1b) reveals a clear separation between the two datasets. Within each cohort, seven well-defined clusters emerge, each corresponding to one of the pacing sites. Clusters associated with the same pacing location in Datasets A and B do not overlap but instead form displaced pairs in the latent space. This consistent displacement provides visual evidence of a domain shift between the cohorts, arising not from physiological differences, but from systematic variations in anatomical distributions, acquisition protocols, or preprocessing pipelines. This domain shift has a measurable impact on cross-domain generalisation performance. The methodology used to assess this effect is detailed in Methods.

We next quantified the primary determinants of total activation time across all simulations. Three factors exert the strongest influence: pacing site, LA surface area, and conduction velocities. The maximum LAT varies across pacing locations in Dataset A (Fig. 1c) and Dataset B

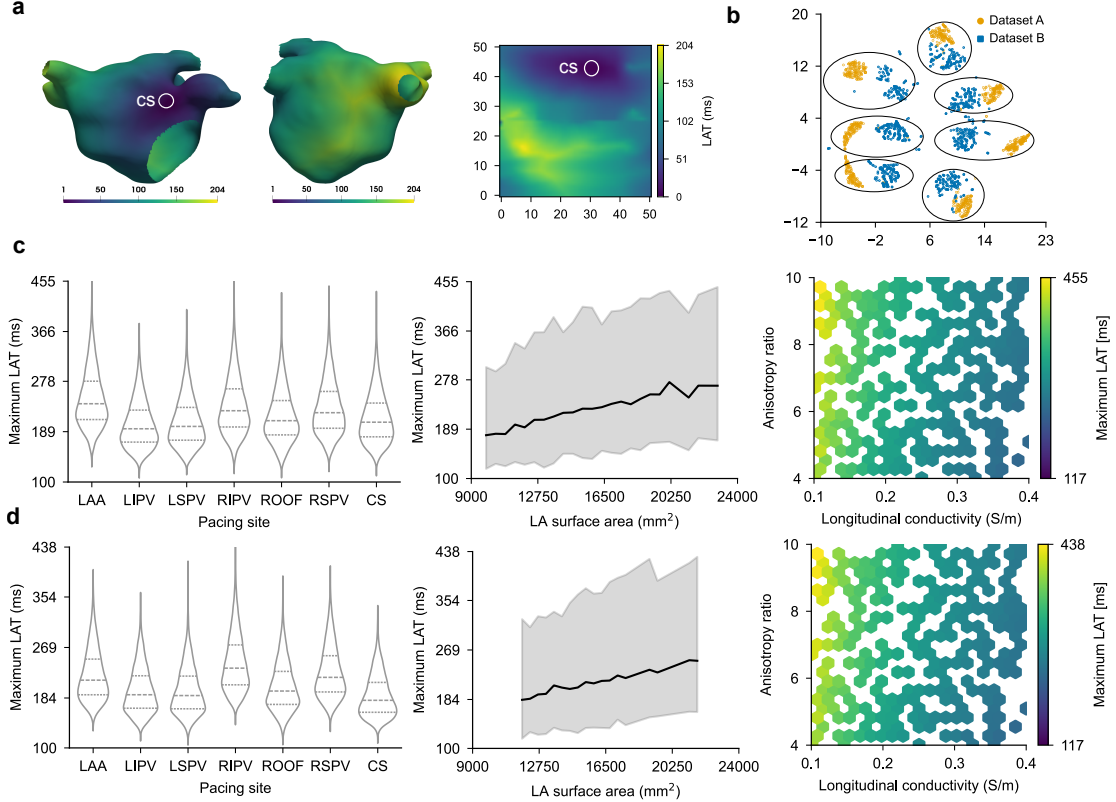


Fig. 1 Construction and characterisation of large-scale electrophysiology datasets generated from biophysically detailed simulations. a, Example local activation time (LAT) map from a 3D left atrium (LA) electrophysiology simulation with coronary sinus pacing, together with its projection onto the standardised Universal Atrial Coordinate (UAC) domain. **b**, UMAP embedding of all UAC-projected LAT maps from Datasets A and B, showing seven pacing-site clusters per cohort and systematic displacement between corresponding clusters, indicating a pronounced domain shift between the two datasets. **c**, Distribution of maximum LAT across pacing locations in Dataset A, demonstrating linear dependence on LA surface area and sensitivity to conductivity. **d**, Corresponding analysis for Dataset B, showing the same physiological trends despite cohort-level differences.

(Fig. 1d). Across both datasets, maximum LAT increases approximately linearly with LA surface area and decreases with increasing conductivity values. These consistent trends confirm that surface area and conductivity jointly modulate global activation timing, motivating their inclusion as key anatomical features in the subsequent analyses.

Input feature sensitivity analysis

We quantified the contribution of individual anatomical input modalities by systematically removing spatial coordinates, fibre orientation, and surface area features, retraining the model under each configuration. Model performance was evaluated using mean absolute error (MAE), which captures numerical accuracy in milliseconds, and the structural similarity index measure (SSIM) [32], which assesses spatial fidelity of the predicted activation maps. All results are

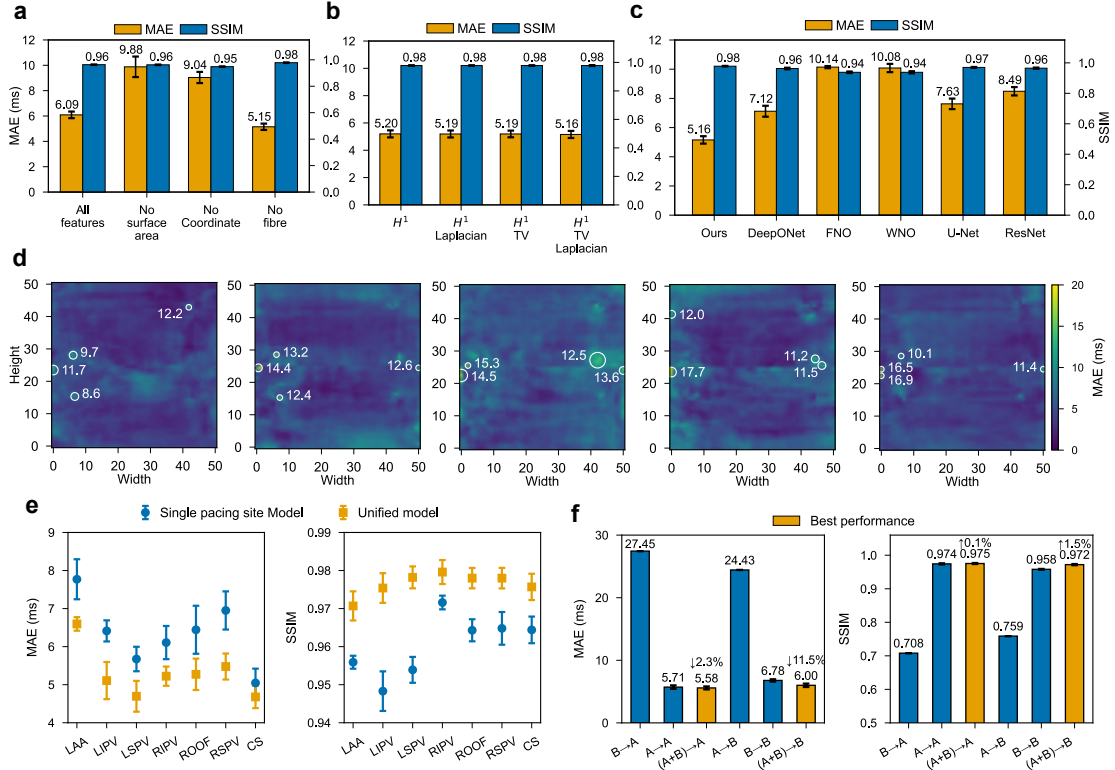


Fig. 2 Comprehensive evaluation of model performance for LAT map prediction. **a**, Our model performance from feature sensitivity tests on Dataset A, demonstrating the contribution of each input feature. **b**, Evaluation of the impact of two regularisation terms, namely total variance (TV) and Laplacian, on LAT map prediction on Dataset A. **c**, Performance comparison between our proposed model and established deep learning architectures, including DeepONet, Fourier Neural Operator (FNO), Wavelet Neural Operator (WNO), U-Net, and ResNet on Dataset A. **d**, Spatial distribution of the averaged LAT prediction error (in ms) across five test cases in a representative validation fold. White circles highlight regions with the highest prediction errors, and adjacent numbers show the average error within those specific regions. **e**, Performance comparison between Single Pacing Location Models and a Unified Model across seven pacing sites. **f**, Cross-domain performance comparison on two distinct datasets. The notation $X \rightarrow Y$ indicates that the model was trained on source dataset X and evaluated on target dataset Y .

reported using five-fold cross-validation. Unless otherwise stated, experiments were conducted on Dataset A, with cross-domain evaluations involving both Datasets A and B.

As shown in Fig. 2a, incorporating all anatomical features yields accurate and spatially coherent predictions of local activation time. Removing the surface area feature leads to a substantial degradation in performance, highlighting the importance of global anatomical scaling for correctly organising activation wavefronts. Similarly, excluding spatial coordinates significantly reduces both numerical accuracy and structural similarity, demonstrating that explicit localisation in the UAC domain is essential for resolving conduction pathways.

In contrast, removing fibre orientation features unexpectedly improves predictive performance across both metrics. This observation indicates that, in the present formulation, fibre orientation does not provide an additional informative signal beyond that already captured by geometric coordinates and global anatomical features. Based on this result, fibre orientation inputs were excluded from all subsequent experiments. Explanations for this effect are discussed further below.

Evaluating the effect of regularisation

We investigated the impact of spatial regularisation on LAT map reconstruction by augmenting the H^1 loss with two commonly used smoothness terms: total variation (TV) and a second-order Laplacian penalty, applied individually or in combination. These regularisation terms are designed to suppress high-frequency artefacts while preserving physiologically meaningful spatial structure.

Model performance was evaluated across a range of regularisation strengths ($\lambda \in \{5 \times 10^{-2}, 3 \times 10^{-2}, 1 \times 10^{-2}, 5 \times 10^{-3}, 1 \times 10^{-3}\}$) using five-fold cross-validation. For each configuration, performance metrics were averaged across folds and regularisation weights to isolate the effect of the regularisation formulation (Fig. 2b).

Among all tested configurations, combining the H^1 loss with both TV and Laplacian regularisation consistently yielded the best performance, achieving the lowest mean MAE and highest SSIM. This result indicates that jointly enforcing first- and second-order smoothness constraints enhances structural fidelity without sacrificing numerical accuracy. In contrast, applying either TV or Laplacian regularisation alone resulted in smaller and less consistent improvements, suggesting that their combined effect is necessary to adequately capture the spatial organisation of activation patterns.

Benchmarking model performance

We benchmarked our approach against a range of neural operators and convolutional architectures commonly used for modelling cardiac activation from multimodal inputs. To ensure a fair comparison, models were evaluated across approximately capacity-matched configurations spanning representative hyperparameter ranges (Fig. 2c). Full architectural details and exhaustive results are provided in Supplementary Section 2 and Supplementary Table 1.

Among operator learning methods, the Fourier Neural Operator (FNO) and Wavelet Neural Operator (WNO) exhibited limited empirical performance in this setting, indicating challenges in capturing heterogeneous and noisy electrophysiological patterns on complex anatomical domains. DeepONet, implemented using our ViT-based backbone for both branch and trunk networks, achieved substantially improved accuracy, reflecting its stronger capacity to model global functional relationships.

Convolutional baselines showed a similar trend. The U-Net architecture outperformed the simpler ResNet model, consistent with its multi-scale encoder-decoder structure and strong inductive bias for spatial localisation. Nevertheless, convolutional models remained limited in their ability to capture global pacing effects and long-range spatial dependencies.

Our model outperformed all baselines, achieving the highest numerical accuracy and structural fidelity across all evaluated metrics. This result demonstrates its superior ability

to integrate heterogeneous anatomical and physiological inputs into spatially coherent and physiologically consistent LAT predictions.

To assess where residual errors concentrate spatially, we visualised prediction error distributions across the UAC domain (Fig. 2d). Across representative test cases, errors are predominantly localised to a narrow horizontal band corresponding to the UAC seam, while remaining low and diffuse elsewhere, indicating high fidelity across most anatomical regions.

Beyond accuracy, we evaluated computational efficiency to assess suitability for real-time applications. On a modern NVIDIA GPU, the model achieved an average inference time of approximately 0.12 ms per sample. This represents orders of magnitude acceleration relative to conventional finite-element electrophysiology solvers, enabling near real-time LAT prediction across diverse anatomies and pacing configurations.

Model generalisation across pacing sites

Generalisation across diverse pacing conditions is critical for scalable and clinically useful prediction of atrial activation, as it determines whether a single model can match or exceed the performance of models trained for individual pacing sites. A model that performs well across pacing sites indicates that it has learned shared electrophysiological structure rather than site-specific patterns.

We thus assessed the predictive performance of two modelling paradigms for LAT map reconstruction: (i) Single Pacing Location Models, trained independently for each of seven pacing sites, and (ii) a Unified Model, trained jointly across all sites to learn a shared inductive bias over anatomical and physiological structure. Across all pacing conditions, the Unified Model yields consistent and statistically significant improvements over its independently trained counterparts. Specifically, it achieves a 16.5% reduction in mean MAE from 6.3 ms to 5.2 ms (Fig. 2e, left), demonstrating enhanced predictive accuracy across heterogeneous inputs. The model also delivers a 1.67% increase in average SSIM from 0.960 to 0.976 (Fig. 2e, right), reflecting superior preservation of spatial structure and clinically relevant activation patterns.

The challenge of latent data heterogeneity

Our initial experiments confirmed the strong performance of our model on a single dataset (Dataset A), demonstrating its ability to capture anatomical features relevant to the target task within a controlled domain. However, high performance within the same dataset does not guarantee translational reliability. Here, we distinguish between internal performance, which measures the model's accuracy when trained and tested on the same dataset, and cross-domain performance, which measures generalisation to an independent dataset. Evaluating both is critical to determine whether the model has learned biologically meaningful features or relies on dataset-specific cues.

Cross-domain generalisation was evaluated on two levels. First, we measured model performance when trained and tested on the same dataset (internal performance: $A \rightarrow A$ and $B \rightarrow B$) compared with performance when trained on one dataset and tested on the other (cross-domain performance: $A \rightarrow B$ and $B \rightarrow A$). Second, we assessed whether including data from an additional domain ($(A + B) \rightarrow A$, $(A + B) \rightarrow B$, and $(A + B) \rightarrow (A + B)$) during training improves generalisation to the original dataset, using internal performance as a baseline.

Each evaluation was performed on models trained with 18 combinations of hyperparameters to ensure statistical significance, with results highlighting consistent trends (Fig. 2f; full results are provided in Supplementary Tables 2 and 3). The strong internal performance confirms that the UAC projection effectively separates anatomical representation from patient-specific shape. In contrast, the pronounced drop in cross-domain performance provides clear evidence of latent bias. The model relies on image-specific cues that mislead predictions when applied to a new domain. This finding highlights a second-order challenge in translational modelling. Models are highly sensitive to systematic variations in data representation and annotation rather than true anatomical differences.

Integrating heterogeneous datasets during training mitigates these domain-specific biases. Training on the combined datasets ($A+B$) encourages the model to focus on consistent anatomical features, ignoring spurious correlations tied to individual acquisition or annotation pipelines. Across both datasets, MAE decreased, and SSIM increased in comparison with the internal performance, demonstrating that exposure to independent cohorts acts as a form of regularisation. For completeness, we also evaluated the model trained and tested on the combined datasets $(A+B) \rightarrow (A+B)$, obtaining (5.77 ± 0.16) for MAE and (0.9734 ± 0.003) for SSIM.

Interpolation to patient-specific geometry

To assess anatomical prediction fidelity after interpolation, we evaluated model performance on both LA surface meshes and left ventricular (LV) volume meshes (Fig. 5). Predictions produced in the intrinsic anatomical coordinate domain were interpolated back onto the original patient-specific mesh geometry, enabling anatomically faithful reconstruction in both settings.

Model performance was evaluated using a previously proposed benchmark task in which LAT is predicted from one of seven pacing locations alone [27]. Our experiments were conducted on Cohort A using 100 left atrial geometries, of which 20 were held out for testing. In addition, 1,006 left ventricular (LV) meshes were obtained from a publicly available dataset [33], with 106 meshes reserved for evaluation. Model inputs and outputs were represented on a 100×100 grid for LAs and a $50 \times 50 \times 50$ volumetric grid for LVs.

On test data, the model achieves mean absolute errors of 5–6 ms for LA geometries, relative to maximum activation times of up to 285 ms. For LV geometries, errors are consistently lower, typically ranging between 2 and 4 ms for maximum activation times of up to 350 ms. These ventricular error levels improve upon those reported in prior geometry-independent operator learning approaches, where mean absolute errors of approximately 5–6 ms were observed for LV meshes [27]. In both atrial and ventricular settings, errors remain consistent across pacing locations, indicating stable performance independent of stimulation site. Spatially, elevated errors in the LA are primarily localised to the atrial appendage and pulmonary vein openings, regions characterised by complex geometry and boundary effects. For the LV, larger errors are observed near the basal openings, corresponding to truncation at the valve plane, and along the interface with the right ventricle, reflecting geometric discontinuities introduced during extraction from bi-ventricular meshes.

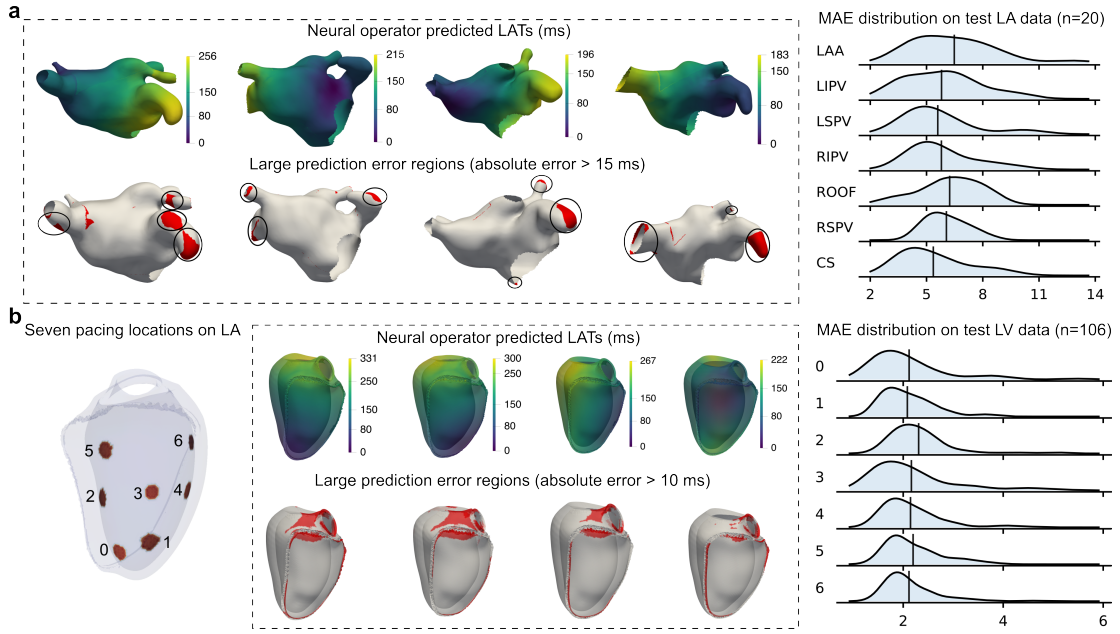


Fig. 3 Interpolation of neural operator predictions to patient-specific atrial and ventricular mesh geometries. **a**, Left: local activation time (LAT) predictions interpolated from the coordinate domain back onto representative left atrial (LA) surface meshes. Regions where the absolute prediction error exceeds 15 ms are highlighted. Right: distribution of mean absolute error across pacing locations evaluated on 100 LA test cases. **b**, Corresponding results for left ventricular (LV) meshes, showing interpolated LAT predictions, regions of large absolute error, and error distributions across pacing locations.

Discussion

Geometry-independent neural operator learning

Our approach demonstrates that a well-designed coordinate system is an efficient tool for bridging the gap between irregular, real-world data and the structured-domain requirements of neural networks, allowing a single neural operator to learn a geometry-independent mapping. By leveraging the universal coordinate system, we established a canonical representation that enabled neural operators to robustly capture the complex, nonlinear physics of cardiac conduction [34–37]. The resulting prediction accuracy, with mean absolute errors on the order of 5 ms, lies within the typical measurement uncertainty and physiological variability reported for clinical electroanatomic mapping systems [38] (typically on the order of 5–10 ms [39]). This demonstrates that our model’s predictions are not only numerically accurate but also fall within a clinically acceptable margin.

A central premise of this work is that effective neural operator learning in cardiac electrophysiology depends on access to large, diverse, and high-quality training data. To this end, we developed a GPU-accelerated finite element electrophysiology solver that enables efficient generation of high-fidelity simulations across a wide range of patient-specific left atrial anatomies and electrophysiological conditions. This data generation pipeline addresses a longstanding

computational bottleneck in cardiac modelling and provides a scalable foundation for learning generalisable electrophysiological structure.

Beyond supporting our framework, this large, curated dataset provides a foundation for future data-driven studies in cardiac electrophysiology. Its scale, diversity, and consistency enable predictive models to generalise across anatomies and protocols, a capability previously limited by data scarcity. For context, G-FuNK [40] was trained on 25 left atrial geometries, while DIMON [27] leveraged 1,006 ventricular geometries simulated at multiple pacing sites. In contrast, our simulations preserve these locations while also varying tissue conductivity, allowing neural operators to capture electrophysiological responses across diverse stimulation patterns and heterogeneous, patient-specific left atrial anatomies. Overall, our dataset spans 308,700 simulations, offering a far richer foundation for training and benchmarking state-of-the-art neural operators.

The observation that removing fibre orientation features improved model performance was initially counterintuitive. Our analysis suggests two primary reasons for this finding. First, the current representation of fibre orientation may contain inherent noise or inaccuracies that interfere with the model’s ability to learn the true underlying electrophysiological dynamics. Second, the model appears to be leveraging the spatial and geometric priors provided by the coordinates and surface area features more effectively. These geometric inputs may implicitly contain sufficient information about the overall anatomical structure, making the explicit fibre orientation data redundant or even counterproductive in its current form.

Comparative model analysis

Our model achieves the best performance, which can be attributed to two key factors. First, the self-attention mechanism enables global context modelling [41], allowing the network to capture long-range dependencies such as conduction wavefront spread from distant pacing sites. Second, by using convolutional patch embeddings and transposed convolution decoding, ViT maintains strong spatial localisation [42], which is critical for resolving the high-frequency components of activation fronts. This balance between global awareness and local detail explains ViT’s superior pointwise accuracy and its strong preservation of spatial gradients.

We benchmarked our approach against several state-of-the-art neural operators and two different CNN architectures. Our model’s performance surpassed these baselines for reasons rooted in their fundamental design. For instance, DeepONet, which in this work employs our model for its branch or trunk networks, leverages the same global context modelling advantages as our model. This enables DeepONet to perform reasonably well, particularly in SSIM and H^1 loss, by effectively capturing smooth functional mappings and spatial dependencies. However, despite incorporating ViT components, DeepONet’s architecture focuses on decomposing input-output relationships into branch and trunk networks, which may limit its end-to-end spatial locality learning compared to the full ViT model. Consequently, its MAE performance lags behind ViT, reflecting some difficulty in the precise localisation of rapid feature changes critical for accurate cardiac wavefront propagation. In contrast, FNOs are designed to learn global mappings in function space using spectral convolutions. While FNOs can capture global trends efficiently, their reliance on low-frequency Fourier modes makes them ill-suited for capturing sharp transitions and local gradient variations common in LAT maps, particularly near pacing initiation sites. This is reflected in their relatively poor H^1 loss and MAE, despite modest SSIM performance. WNOs attempt to address this by incorporating multi-resolution representations,

theoretically improving sensitivity to localised patterns. However, WNO’s performance degrades substantially in this setting, likely due to instability in wavelet decomposition on structured but irregular biomedical domains and sensitivity to small-scale alignment errors, leading to high variance in H^1 loss.

Among the convolutional baselines, U-Net delivers strong SSIM, indicating that it generates visually plausible LAT maps. Its hierarchical multi-scale architecture with skip connections allows for reconstruction of structural details. However, convolutional models like U-Net and ResNet-style CNN architectures are inherently local in receptive field, making it difficult to capture global pacing effects or subtle long-range interactions without very deep networks or large kernels [43].

Toward domain-invariant generalisation

Prior studies have evaluated model performance primarily under variations in pacing site [27]. In contrast, a central contribution of our work is demonstrating that a single model can generalise across both diverse pacing locations and simulation parameters. This capability is essential for clinical applicability, since the pacing site is often variable or unknown in practice. Our results also show that the unified model, trained jointly across all seven pacing sites, consistently and significantly outperforms models trained for individual pacing locations. The unified model achieves a 16.5% reduction in mean MAE, and a 1.6% increase in average SSIM. This demonstrates that our model effectively extracts generalizable electrophysiological principles that are independent of the specific pacing location, making it a robust and scalable solution for real-world clinical applications where prior knowledge of the stimulation site is unavailable.

Our cross-domain experiments reveal a critical insight. The apparent limitation of single-domain models is not a shortcoming of the ViT architecture, but a reflection of latent heterogeneity in clinical imaging data. By explicitly combining datasets from distinct acquisition and annotation protocols, we demonstrate that the model naturally discards protocol-specific shortcuts and focuses on the fundamental anatomical structure. This approach not only rescues performance on external cohorts but also slightly improves internal predictions.

This finding establishes a generalizable strategy for achieving domain-invariant medical image analysis. The universal coordinate projection provides the necessary geometry-invariant foundation, while training on heterogeneous data acts as a regularisation method in feature space, compelling the model to learn only the biophysically relevant structures common to both domains and emphasising that true translational power derives from integrating diverse, multi-centre data rather than from isolated single-site optimisation.

Limitations and future directions

Beyond feature representation, limitations also arise from the use of intrinsic anatomical coordinate systems. For the left atrium, the UAC system maps a closed, topologically complex three-dimensional surface onto a flat two-dimensional domain. This flattening necessarily requires introducing a cut line on the surface, which appears as a seam in the coordinate representation. As a result, points that are physically adjacent on the original anatomy become separated across this seam, creating an artificial spatial discontinuity for the learning model.

Consistent with this construction, our results reveal a narrow, coherent band of elevated prediction error aligned with the UAC seam, indicating that the neural operator struggles to interpolate smoothly across this boundary.

In addition to seam-related effects, further localised errors are observed in regions of pronounced anatomical and electrophysiological complexity, particularly around the pulmonary vein junctions and the left atrial appendage. These regions exhibit substantial inter-patient variability that cannot be fully normalised by the UAC projection, leading to residual geometric heterogeneity in the coordinate domain. Moreover, activation wavefronts in these areas often display steep local gradients in activation time, increasing sensitivity to small spatial misalignments. Together, these factors likely contribute to the small but systematic clusters of elevated error observed in physiologically critical regions. These observations indicate that while the proposed framework captures global activation patterns and long-range structure effectively, resolving fine-scale, anatomy-driven variations remains challenging.

By contrast, ventricular geometries parameterised using the UVC do not exhibit a comparable global seam-induced discontinuity. Instead, elevated errors are primarily confined to regions introduced by geometric truncation, such as the basal valve plane and the interface with the right ventricle. This contrast highlights that coordinate-induced limitations are strongly dependent on underlying anatomical topology rather than intrinsic to the operator-learning framework itself, and that intrinsic coordinate representations may behave differently across cardiac chambers.

Finally, the framework was trained exclusively on high-fidelity simulated datasets. Although these simulations span a wide range of anatomies and electrophysiological parameters, validation against clinical electroanatomic mapping data will be essential to assess robustness under real-world conditions. In addition, the current implementation focuses primarily on atrial and ventricular geometries in isolation; extending the approach to whole-heart or fully biventricular modelling will require adapting the anatomical parameterisation and scaling the data generation process. Future directions include integrating hybrid simulation–clinical datasets, refining anatomical representations in regions of high complexity, and exploring adaptive spatial resolution strategies to further improve local accuracy without compromising inference efficiency.

Methods

We describe a computational framework that combines high-fidelity electrophysiology simulations with neural operator learning to enable efficient prediction of LAT maps (Fig. 4).

Image data processing

Datasets description

The full dataset comprised 147 patient-specific left LA anatomies derived from two large-scale clinical cohorts. These anatomies served both as inputs to the EP simulations and as training and evaluation data for the neural operator models. To support both internal evaluation and cross-domain generalisation analysis, the 147 anatomies were partitioned into two distinct cohorts (Cohort A and Cohort B).

Cohort A, consisting of 100 AF LA samples (43 paroxysmal, 41 persistent, and 16 long-standing persistent), was obtained from the AF Recurrence Cohort [44], which was recruited in London, UK. LA geometries were segmented from late gadolinium-enhanced cardiac magnetic

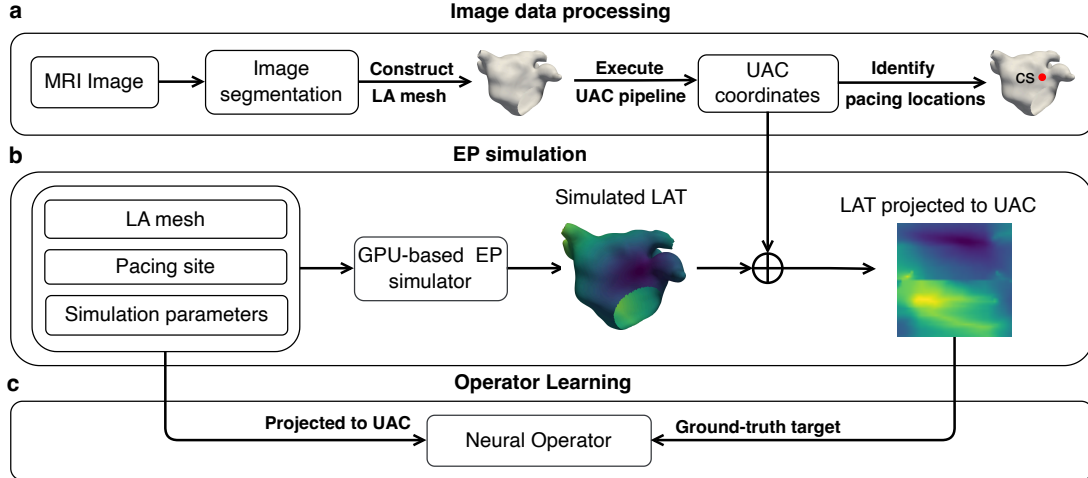


Fig. 4 The overview of our proposed computational framework for operator learning for electro-physiology (EP) simulations. **a**, Preparation of left atrium (LA) mesh, mapping the 3D vertex coordinates defining the mesh to a 2D grid by Universal Atrial Coordinates (UAC), and identifying the pacing locations. **b**, The application of our GPU-based FEM solver to produce a large amount of simulated local activation time (LAT) maps, which are also projected to 2D grids by UAC. **c**, The training of neural operators using the structured simulation data.

resonance (LGE-CMR) images acquired at end-diastole, yielding three-dimensional anatomical surfaces including the pulmonary veins and mitral annulus. Fibrotic tissue distribution was quantified using standard LGE intensity thresholding, providing patient-specific fibrosis maps that informed the EP simulations. This cohort served as the controlled domain for model development and internal validation.

Cohort B, containing 47 LA samples from AF patients recruited from Amsterdam, The Netherlands, was sourced from an independent clinical study [45]. The LA geometries in this cohort underwent the same segmentation and fibrosis quantification pipeline as those in Cohort A to maintain structural consistency.

As LGE-CMR does not resolve myofibre orientation, fibre direction vectors for anisotropic conduction were generated for all 147 anatomies using a model based on high-resolution ex-vivo Diffusion Tensor Magnetic Resonance Imaging (DTMRI) data [46]. These fibre fields were subsequently incorporated into an atrial fibre atlas and projected onto each patient-specific geometry using the UAC system, as described by [47].

Notably, Cohorts A and B were derived from two distinct and independent studies conducted by separate research groups operating within independent healthcare systems. This independence in data acquisition and analysis supports robust cross-domain evaluation. Moreover, despite adhering to equivalent segmentation and processing workflows [48, 49], the two cohorts exhibit meaningful domain shifts. Variations arise from MRI acquisition parameters (scanner vendor, pulse sequences, and field strength), from different practices in anatomical trimming (particularly of pulmonary veins and the LA appendage), and from inter-operator differences in anatomical landmarking and boundary definitions. These protocol-level and anatomical choices shape the resulting geometries and fibrosis patterns, such that models trained exclusively on

Cohort A typically encounter Cohort B as an out-of-distribution domain. These differences are not physiological changes. These differences are not physiological. They are artefacts of data preparation, yet they change the geometric domain on which the operator is defined.

Universal coordinates projection

Spatial coordinates, fibre directions, and LAT fields from patient-specific mesh geometries are projected onto structured grids of fixed resolution using universal anatomical coordinate systems. For the left atrium, UAC defines a bijective transformation

$$\Phi_{\text{LA}} : \mathcal{M} \rightarrow [0, 1]^2,$$

where $\mathcal{M} \subset \mathbb{R}^3$ denotes the atrial surface manifold. The mapping is constructed from anatomical landmarks, including the pulmonary vein junctions and mitral annulus, yielding a geodesic distance-based unfolding that aligns corresponding anatomical regions across patients [28]. An analogous intrinsic parameterisation is applied to ventricular geometries using the UVC system, which maps the three-dimensional ventricular volume to a structured coordinate domain.

Let $f : \mathcal{M} \rightarrow \mathbb{R}$ denote a scalar field on the mesh (e.g., LAT), and let $\xi_i = \Phi(\mathbf{x}_i)$ be the corresponding UAC or UVC coordinates of mesh point \mathbf{x}_i . A coordinate-domain representation \tilde{f} is constructed via spatial interpolation,

$$\tilde{f}(\xi) = \mathcal{I}(\{(\xi_i, f_i)\}_{i=1}^N),$$

where $\mathcal{I}(\cdot)$ combines linear interpolation in densely sampled regions with nearest-neighbour interpolation near anatomical boundaries.

For atrial meshes, three-dimensional vertex coordinates (x, y, z) are mapped to a grid in the UAC domain. Fibre orientations, originally defined per element, are converted to vertex-wise vectors using area-weighted averaging and normalised to unit length before projection. An equivalent procedure is applied in the UVC domain for ventricular geometries. After neural operator inference in the coordinate domain, predictions can be mapped back to the original patient-specific geometry. For each mesh point $\mathbf{x} \in \mathcal{M}$ with coordinate $\xi = \Phi(\mathbf{x})$, the predicted value is recovered by interpolating the learned field $\tilde{f}(\xi)$.

Identify pacing locations

To ensure the generalisability of neural operators and to capture a wide range of conduction dynamics, the EP simulations were initiated using a distributed set of seven clinically relevant pacing sites in the LA: the Left Atrial Appendage (LAA), the Left Superior and Inferior Pulmonary Veins (LSPV, LIPV), the Right Superior and Inferior Pulmonary Veins (RSPV, RIPV), the Coronary Sinus (CS), and the Roof which is defined as the superior wall of the left atrium connecting the LSPV and RSPV [50–52].

Pacing locations are defined across all patient anatomies using the UAC system. For each anatomical region, a 2D bounding box within the UAC domain was specified, delineating a subset of mesh vertices. The physical pacing centre is computed as the mean position of all vertices within that UAC-defined box. The stimulation region is subsequently defined by all mesh vertices located within a fixed Euclidean radius of 2.0 mm from this central point, ensuring

comparable stimulation volumes across all seven sites. The spatial distribution of these seven sites on a representative LA mesh is mapped onto the UAC coordinate system in Fig. 5.

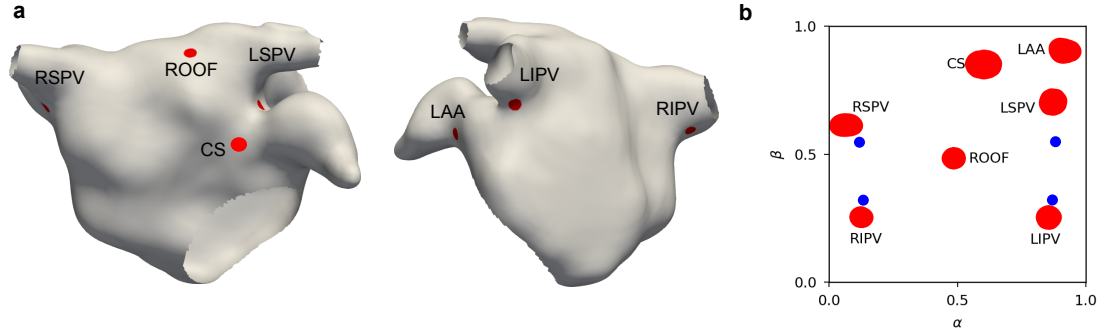


Fig. 5 Marking pacing sites on an LA. **a**, Anterior and posterior views of an LA mesh where the seven pacing locations have been marked. **b**, Spatial distribution of these pacing sites in UAC coordinates. The blue regions indicate the anatomical openings (pulmonary veins and mitral valve).

GPU-based FEM EP simulation

To generate a large-scale, comprehensive dataset for training, we simulated LA electrical propagation using the widely adopted monodomain equation [53] (further implementation details are provided in Supplementary Section 1, with an example of simulated wavefront propagation shown in Supplementary Fig. 1 and benchmark verification results in Supplementary Fig. 2). This biophysical model captures the electrical conduction through anisotropic cardiac tissue, balancing capacitive and ionic currents with diffusive current flow, governed by the longitudinal (σ_l) and transverse (σ_t) conductivities.

The primary and clinically significant output extracted from these simulations is the LAT map, which defines the time t at which the transmembrane potential V first crosses a predefined threshold (V_{th} , typically 0 mV) at any location x in the cardiac domain:

$$\text{LAT}(x) = \min \{t > 0 \mid V(x, t) > V_{th}\},$$

For each patient, we varied the longitudinal (σ_l) and transverse (σ_t) conductivities across seven clinically relevant pacing locations. At each pacing site, 300 combinations of σ_l and the anisotropy ratio σ_l/σ_t were sampled using Latin hypercube sampling [30]. The chosen range of σ_l (0.1–0.4 S/m) is consistent with experimentally measured conduction velocities and previously reported myocardial conductivity values [54], while anisotropy ratios between 4 and 10 reflect the substantially faster fibre-aligned conduction observed in atrial tissue [55]. These values imply corresponding σ_t in the range 0.01–0.1 S/m.

Each simulation was run for 600 ms to capture the full activation sequence, and the LAT map was recorded during runtime. Each simulation required approximately one minute on an NVIDIA A100 GPU, enabling the generation of 210,000 simulations for Cohort A and 98,700 simulations for Cohort B, yielding a combined total of 308,700 simulations. Executing these

simulations across eight A100 GPUs reduced the total wall-clock time from an estimated 214 days (single GPU) to approximately 27 days.

Neural operator learning

We formulate LAT map prediction as a neural operator learning problem, in which the goal is to approximate a mapping from patient-specific anatomical and electrophysiological parameters to the corresponding spatial distribution of activation times. Formally, we aim to learn an operator

$$\mathcal{G} : (A, \sigma, p) \mapsto \text{LAT}(\mathbf{x}),$$

where A denotes the atrial geometry, σ the conductivity tensor, p the pacing site location, and $\text{LAT}(\mathbf{x})$ the activation time at position $\mathbf{x} \in \Omega$ where Ω is the computational domain. This framework requires the generation of large and diverse training datasets that pair input configurations (A, σ, p) with ground-truth LAT maps obtained from high-fidelity EP simulations.

Model architecture

Our proposed architecture integrates a coordinate embedding module for point cloud projection with a Vision Transformer-based encoder and a convolutional decoder, enabling high-fidelity spatial field prediction from both sparse and structured physiological data. The model is designed to process heterogeneous inputs, including sparse point clouds (e.g., pacing coordinates) and spatially distributed scalar fields (e.g., tissue conductivity, surface area), by transforming them into a unified, fixed-resolution tensor representation suitable for transformer-based spatial modelling (Fig. 6).

Point-to-grid projection.

To encode pacing (stimulation) locations provided as sparse, unordered two-dimensional point clouds of shape $(N, 2)$ where N is the number of vertices in the pacing region, we introduce an embedding module that maps the point set into a 2D grid representation (Fig. 6b). This module follows the architectural design of PointNet [57], applying a multi-layer perceptron (MLP) independently to each input point, followed by a permutation-invariant mean pooling operation to obtain a global descriptor of the stimulation pattern. This descriptor is then decoded via a learnable mapping to a 2D spatial grid of shape $(3, 50, 50)$. Unlike PointNet, which is optimised for classification and segmentation tasks, our adaptation is explicitly designed to produce spatially structured embeddings that are compatible with convolutional and transformer-based feature extractors.

Multi-modal feature integration.

The input to the neural operator is a multi-modal, multi-channel grid that encodes patient-specific mesh properties and simulation parameters into a fixed-size ten-channel representation (Fig. 6a), which can be divided into two groups. The first group comprises the seven geometric and anatomical channels, including the UAC-projected 3D vertex coordinates (x, y, z) and the 3D fibre direction vectors (six channels in total, each forming a $(3, 50, 50)$ feature map). This is supplemented by the total surface area of the left atrium, a global anatomical feature that is broadcast across the spatial domain to form a $(1, 50, 50)$ constant grid. The second group

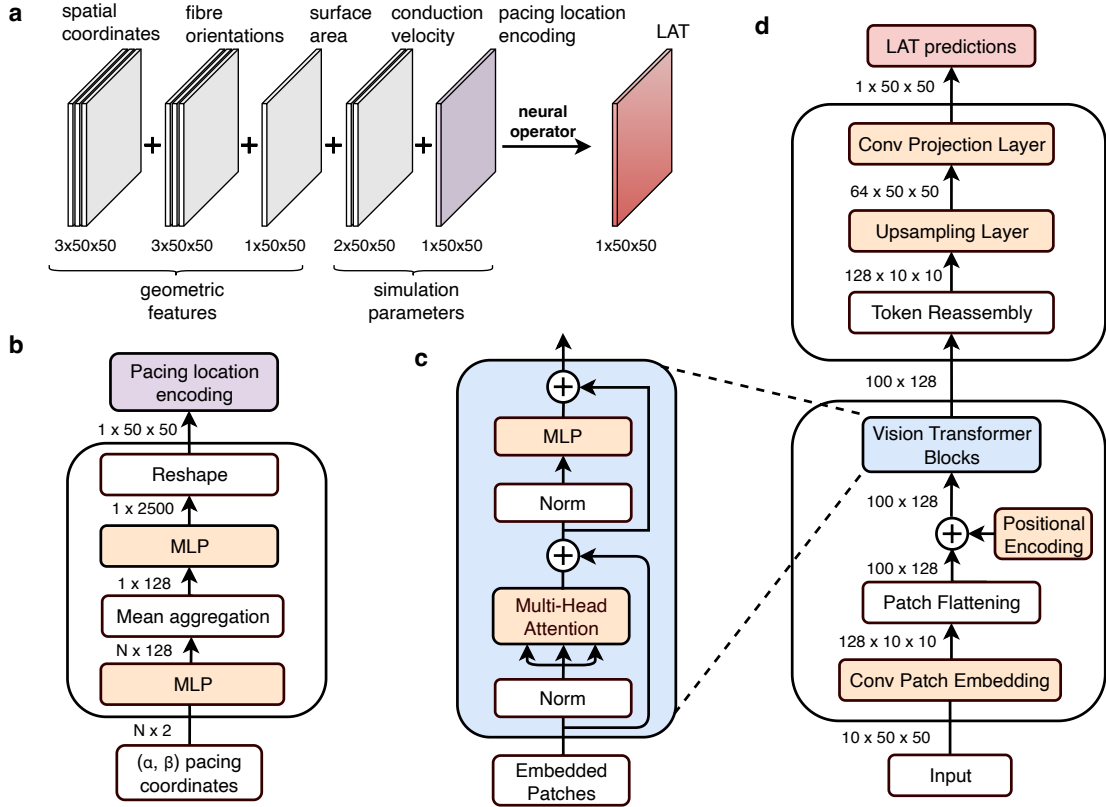


Fig. 6 Model architecture. **a**, The construction of the input and output for neural operator learning, where patient-specific anatomical and physiological parameters are projected onto a structured grid via the Universal Atrial Coordinate system. The pacing location is converted from a point cloud representation into a spatial distribution on the same grid, enabling consistent integration with other input modalities. **b**, A neural network module that maps a point cloud of shape $(N, 2)$, representing spatial input features such as pacing sites or anatomical landmarks, into a structured 2D grid of shape $(1, 50, 50)$. Here, N refers to the number of vertices where stimulus (pacing) is applied. **c**, The Vision Transformer block used in **(d)**, which is the original ViT model proposed in [56]. **d**, Our full encoder-decoder architecture, which uses convolutional patch embedding and a Vision Transformer encoder to process the input grid, and then upsamples the latent features using a transposed convolution and projects them into the final LAT map using a convolutional output layer.

comprises the two parametric features including the two conduction velocities (σ_l and σ_t), which are also broadcast across the spatial domain to form a $(2, 50, 50)$ feature map, and the encoded pacing location in a $(1, 50, 50)$ feature map. The output of the neural network is trained against the target LAT map of shape $(1, 50, 50)$.

ViT-Based Spatial Representation Learning.

To model spatial dependencies across the input domain, we employ a Vision Transformer architecture that encodes the multi-channel input grid into a sequence of contextualised latent representations. A convolutional patch embedding layer [58] first divides the input grid into

non-overlapping patches and projects each patch into a shared embedding space, producing a sequence of latent tokens. Learnable positional embeddings are added to retain spatial structure within the tokenised representation. This sequence is then processed by a stack of standard ViT blocks, each comprising multi-head self-attention and feed-forward sublayers, which enables the integration of global context and the capture of long-range spatial interactions (Fig. 6c).

Following the ViT-based encoder, the latent tokens are reshaped into a compact 2D feature map. To recover full spatial resolution, we employ a lightweight decoder consisting of a transposed convolution layer for upsampling, followed by a convolutional projection head that produces the final output map. The transposed convolution operation, originally introduced in deep learning by [59] for adaptive deconvolutional networks and later popularised for CNN visualisation by [60], enables learnable upsampling by applying the transpose of the convolution operator. This decoding step ensures that the global features encoded by the transformer are effectively translated back into a high-resolution spatial field for pixel-wise prediction.

Sobolev Loss with Spatial Smoothness Regularisations

To ensure our model produces physiologically consistent LAT maps, we employ an objective function grounded in the relative Sobolev H^1 norm. This choice enforces consistency not only in the predicted values but also in their spatial derivatives, a property essential for accurately modelling continuous and smooth conduction patterns.

To further refine the solution and mitigate non-physical, high-frequency artefacts while preserving sharp wavefront transitions, we incorporate two standard regularisation terms. The first is Total Variation (TV) regularisation \mathcal{L}_{TV} , which penalises the L^1 norm of the image gradient. The second is a Laplacian regularisation $\mathcal{L}_{\text{Laplacian}}$, which promotes harmonicity by penalising spatial curvature (full definitions are provided in Supplementary Section 4).

The overall objective function is defined as a weighted sum:

$$\mathcal{L}_{\text{total}} = \mathcal{L}_{H^1}(u, v) + \lambda \mathcal{L}_{\text{TV}}(u) + \lambda \mathcal{L}_{\text{Laplacian}}(u),$$

where $\mathcal{L}_{H^1}(u, v)$ is the primary loss between the predicted LAT map (u) and the ground truth (v), and the hyperparameter λ controls the strength of the regularisation. This combination ensures that the model's predictions are both highly accurate and physiologically coherent.

Declarations

Funding

This work is supported by the NIHR Imperial Biomedical Research Centre (BRC) and by the British Heart Foundation Centre of Research Excellence (RE/24/130023). SAN is supported by NIH R01-HL152256 and R01-HL162260, ERC PREDICT-HF453 (864055), BHF (RG/20/4/34803), EPSRC (EP/P01268X/1, EP/Z531297/1) and by the Technology Missions Fund under the EPSRC Grant EP/X03870X/1 & The Alan Turing Institute. CR receives funding from the British Heart Foundation (RG/20/4/34803). We acknowledge computational resources and support provided by the Imperial College Research Computing Service.

Data availability

Dataset A used in this study is publicly available on Figshare under the permanent identifier

10.6084/m9.figshare.30712559. Dataset B contains sensitive information and cannot be publicly released due to ethical and privacy restrictions. Access to Dataset B may be requested from the corresponding author and will be provided subject to institutional approval and a formal data-sharing agreement.

Code availability

All code used to generate the results in this study is available at: https://github.com/sagebei/unified_framework_operator_learning.

Author contributions

B.Z. developed the computational methodology, performed simulations, and drafted the manuscript. C.C. contributed to model development and data analysis. S.Q. assisted with numerical experiments and model development. M.B. contributed to software implementation and optimisation. A.W.C.L. prepared the data. C.R. contributed to manuscript editing and provided the simulation data. C.R., M.J.W.G. and L.H.G.A.H. provided experimental data. M.Q. assisted with analysing results. S.N. supervised the study, contributed to conceptualisation, and revised the manuscript. All authors reviewed the manuscript.

Competing interests

The authors declare no competing interests.

References

- [1] Niederer, S. A., Lumens, J. & Trayanova, N. A. Computational models in cardiology. *Nature reviews cardiology* **16**, 100–111 (2019).
- [2] Trayanova, N. A., Lyon, A., Shade, J. & Heijman, J. Computational modeling of cardiac electrophysiology and arrhythmogenesis: toward clinical translation. *Physiological reviews* **104**, 1265–1333 (2024).
- [3] Prakosa, A. *et al.* Personalized virtual-heart technology for guiding the ablation of infarct-related ventricular tachycardia. *Nature biomedical engineering* **2**, 732–740 (2018).
- [4] Williams, S. E. *et al.* Local activation time sampling density for atrial tachycardia contact mapping: how much is enough? *Ep Europace* **20**, e11–e20 (2018).
- [5] Jaffery, O. A., Melki, L., Slabaugh, G., Good, W. W. & Roney, C. H. A review of personalised cardiac computational modelling using electroanatomical mapping data. *Arrhythmia & Electrophysiology Review* **13**, e08 (2024).
- [6] Karoui, A., Bendahmane, M. & Zemzemi, N. Cardiac activation maps reconstruction: a comparative study between data-driven and physics-based methods. *Frontiers in physiology* **12**, 686136 (2021).
- [7] Niederer, S. A. *et al.* Verification of cardiac tissue electrophysiology simulators using an n-version benchmark. *Philosophical Transactions of the Royal Society A: Mathematical,*

Physical and Engineering Sciences **369**, 4331–4351 (2011).

[8] Plank, G. *et al.* The opencarp simulation environment for cardiac electrophysiology. *Computer methods and Programs in Biomedicine* **208**, 106223 (2021).

[9] Sahli Costabal, F., Zaman, J. A., Kuhl, E. & Narayan, S. M. Interpreting activation mapping of atrial fibrillation: a hybrid computational/physiological study. *Annals of biomedical engineering* **46**, 257–269 (2018).

[10] Kornej, J., Börschel, C. S., Benjamin, E. J. & Schnabel, R. B. Epidemiology of atrial fibrillation in the 21st century: novel methods and new insights. *Circulation research* **127**, 4–20 (2020).

[11] Cheng, S. *et al.* Global burden of atrial fibrillation/atrial flutter and its attributable risk factors from 1990 to 2021. *Europace* **26**, euae195 (2024).

[12] Li, X. *et al.* Global burden and health inequality of atrial fibrillation/atrial flutter from 1990 to 2021. *Frontiers in Cardiovascular Medicine* **12**, 1585980 (2025).

[13] Lai, Y. *et al.* Causes of death in patients with atrial fibrillation in the uk: a nationwide electronic health record study. *European heart journal open* **5**, oea103 (2025).

[14] Heijman, J., Sutanto, H., Crijns, H. J., Nattel, S. & Trayanova, N. A. Computational models of atrial fibrillation: achievements, challenges, and perspectives for improving clinical care. *Cardiovascular Research* **117**, 1682–1699 (2021).

[15] Boyle, P. M. *et al.* Computationally guided personalized targeted ablation of persistent atrial fibrillation. *Nature biomedical engineering* **3**, 870–879 (2019).

[16] Roney, C. H. *et al.* Time-averaged wavefront analysis demonstrates preferential pathways of atrial fibrillation, predicting pulmonary vein isolation acute response. *Frontiers in Physiology* **12**, 707189 (2021).

[17] Krogh-Madsen, T., Abbott, G. W. & Christini, D. J. Effects of electrical and structural remodeling on atrial fibrillation maintenance: a simulation study. *PLoS computational biology* **8**, e1002390 (2012).

[18] Niederer, S., Mitchell, L., Smith, N. & Plank, G. Simulating human cardiac electrophysiology on clinical time-scales. *Frontiers in physiology* **2**, 14 (2011).

[19] Kovachki, N. *et al.* Neural operator: Learning maps between function spaces with applications to pdes. *Journal of Machine Learning Research* **24**, 1–97 (2023).

[20] Lu, L., Jin, P., Pang, G., Zhang, Z. & Karniadakis, G. E. Learning nonlinear operators via deeponet based on the universal approximation theorem of operators. *Nature machine intelligence* **3**, 218–229 (2021).

- [21] Li, Z. *et al.* Fourier neural operator for parametric partial differential equations. *International Conference on Learning Representations* (2021).
- [22] Li, Z., Huang, D. Z., Liu, B. & Anandkumar, A. Fourier neural operator with learned deformations for pdes on general geometries. *Journal of Machine Learning Research* **24**, 1–26 (2023).
- [23] Li, Z. *et al.* Geometry-informed neural operator for large-scale 3d pdes. *Advances in Neural Information Processing Systems* **36**, 35836–35854 (2023).
- [24] Ahmad, Z. *et al.* Diffeomorphic latent neural operators for data-efficient learning of solutions to partial differential equations. *arXiv preprint arXiv:2411.18014* (2024).
- [25] Trayanova, N. A., Popescu, D. M. & Shade, J. K. Machine learning in arrhythmia and electrophysiology. *Circulation research* **128**, 544–566 (2021).
- [26] Zhao, Z., Liu, C., Li, Y., Chen, Z. & Liu, X. Diffeomorphism neural operator for various domains and parameters of partial differential equations. *Communications Physics* **8**, 15 (2025).
- [27] Yin, M. *et al.* A scalable framework for learning the geometry-dependent solution operators of partial differential equations. *Nature computational science* **4**, 928–940 (2024).
- [28] Roney, C. H. *et al.* Universal atrial coordinates applied to visualisation, registration and construction of patient specific meshes. *Medical image analysis* **55**, 65–75 (2019).
- [29] Bayer, J. *et al.* Universal ventricular coordinates: A generic framework for describing position within the heart and transferring data. *Medical image analysis* **45**, 83–93 (2018).
- [30] McKay, M. D., Beckman, R. J. & Conover, W. J. A comparison of three methods for selecting values of input variables in the analysis of output from a computer code. *Technometrics* **42**, 55–61 (2000).
- [31] Healy, J. & McInnes, L. Uniform manifold approximation and projection. *Nature Reviews Methods Primers* **4**, 82 (2024).
- [32] Wang, Z., Bovik, A. C., Sheikh, H. R. & Simoncelli, E. P. Image quality assessment: from error visibility to structural similarity. *IEEE transactions on image processing* **13**, 600–612 (2004).
- [33] Ugurlu, D. *et al.* Cardiac digital twins at scale from mri: open tools and representative models from ~ 55000 uk biobank participants. *Plos one* **20**, e0327158 (2025).
- [34] Hao, Z. *et al.* Gnot: A general neural operator transformer for operator learning. *International Conference on Machine Learning* 12556–12569 (2023).
- [35] Li, Z., Meidani, K. & Farimani, A. B. Transformer for partial differential equations' operator learning. *Transactions on Machine Learning Research* (2023).

- [36] Shih, B., Peyvan, A., Zhang, Z. & Karniadakis, G. E. Transformers as neural operators for solutions of differential equations with finite regularity. *Computer Methods in Applied Mechanics and Engineering* **434**, 117560 (2025).
- [37] Ovadia, O. *et al.* Vito: Vision transformer-operator. *Computer Methods in Applied Mechanics and Engineering* **428**, 117109 (2024).
- [38] Gaeta, S., Bahnson, T. D. & Henriquez, C. High-resolution measurement of local activation time differences from bipolar electrogram amplitude. *Frontiers in Physiology* **12**, 653645 (2021).
- [39] Narayan, S. M. & John, R. M. Advanced electroanatomic mapping: current and emerging approaches. *Current Treatment Options in Cardiovascular Medicine* **26**, 69–91 (2024).
- [40] Loeffler, S. E. *et al.* Graph fourier neural kernels (g-funk): Learning solutions of nonlinear diffusive parametric pdes on multiple domains. *arXiv preprint arXiv:2410.04655* (2024).
- [41] Vaswani, A. *et al.* Attention is all you need. *Advances in neural information processing systems* **30** (2017).
- [42] Wang, C. *et al.* Convolutional embedding makes hierarchical vision transformer stronger. *European conference on computer vision* 739–756 (2022).
- [43] Luo, W., Li, Y., Urtasun, R. & Zemel, R. Understanding the effective receptive field in deep convolutional neural networks. *Advances in neural information processing systems* **29** (2016).
- [44] Roney, C. H. *et al.* Predicting atrial fibrillation recurrence by combining population data and virtual cohorts of patient-specific left atrial models. *Circulation: Arrhythmia and Electrophysiology* **15**, e010253 (2022).
- [45] Lee, A. W. *et al.* Is regional atrial strain a useful surrogate of regional atrial fibrosis in atrial cardiomyopathy? *European Heart Journal-Imaging Methods and Practice* **3**, qyaf068 (2025).
- [46] Pashakhanloo, F. *et al.* Myofiber architecture of the human atria as revealed by submillimeter diffusion tensor imaging. *Circulation: arrhythmia and electrophysiology* **9**, e004133 (2016).
- [47] Roney, C. H. *et al.* Constructing a human atrial fibre atlas. *Annals of biomedical engineering* **49**, 233–250 (2021).
- [48] Solís-Lemus, J. A. *et al.* Evaluation of an open-source pipeline to create patient-specific left atrial models: a reproducibility study. *Computers in Biology and Medicine* **162**, 107009 (2023).
- [49] Razeghi, O. *et al.* Cemrgapp: an interactive medical imaging application with image processing, computer vision, and machine learning toolkits for cardiovascular research.

SoftwareX **12**, 100570 (2020).

- [50] Romero, J., Natale, A. & Di Biase, L. Atrial fibrillation ablation beyond pulmonary veins: the role of left atrial appendage. *Revista Portuguesa de Cardiologia* **36**, 31–41 (2017).
- [51] Moreira, W., Timmermans, C., Wellens, H. J. & Rodriguez, L.-M. Atrial tachycardia originating from the pulmonary vein: importance of the stimulation sites. *Texas Heart Institute Journal* **35**, 356 (2008).
- [52] Elmariyah, S. *et al.* Coronary sinus pacing for the management of right ventricular and atrial infarction with isolated right ventricular pulsus alternans. *Texas Heart Institute Journal* **40**, 497 (2013).
- [53] Geselowitz, D. B. & Miller, W. A bidomain model for anisotropic cardiac muscle. *Annals of biomedical engineering* **11**, 191–206 (1983).
- [54] Fu, Z. *et al.* Progress of conductivity and conduction velocity measured in human and animal hearts. *Reviews in Cardiovascular Medicine* **25**, 364 (2024).
- [55] Kotadia, I. *et al.* Anisotropic cardiac conduction. *Arrhythmia & Electrophysiology Review* **9**, 202 (2020).
- [56] Dosovitskiy, A. *et al.* An image is worth 16x16 words: Transformers for image recognition at scale. *International Conference on Learning Representations* (2021).
- [57] Qi, C. R., Su, H., Mo, K. & Guibas, L. J. Pointnet: Deep learning on point sets for 3d classification and segmentation. *Proceedings of the IEEE conference on computer vision and pattern recognition* 652–660 (2017).
- [58] Wu, H. *et al.* CvT: Introducing convolutions to vision transformers. *Proceedings of the IEEE/CVF international conference on computer vision* 22–31 (2021).
- [59] Zeiler, M. D., Taylor, G. W. & Fergus, R. Adaptive deconvolutional networks for mid and high level feature learning. *2011 international conference on computer vision* 2018–2025 (2011).
- [60] Zeiler, M. D. & Fergus, R. Visualizing and understanding convolutional networks. *European conference on computer vision* 818–833 (2014).